HDG-NEFEM for two dimensional linear elasticity

Ruben Sevilla[a,1]

[a] *Zienkiewicz Centre for Computational Engineering, College of Engineering, Swansea University, Swansea, SA1 8EN, Wales, UK.*

Abstract

This paper proposes a new methodology for the solution of two dimensional linear elastic problems in domains with curved boundaries. The proposed method exploits the advantages of the hybridisable discontinuous Galerkin method to obtain an accurate approximation of both the displacement and the stress fields by solving a global problem that only involves the displacement field on the element edges as unknown. In addition, the methodology incorporates the exact boundary representation of the domain by means of the so-called NURBS-enhanced finite element method. Numerical examples are used to illustrate the three main advantages of the proposed method, namely the reproducibility of polynomials in domains with curved boundaries, the super-convergence of the solution even for linear approximation and the effectiveness and reliability of degree adaptive processes driven by displacement or stresses.

Keywords: hybridisable discontinuous Galerkin, NURBS-enhanced finite element method, linear elasticity, curved boundary, degree adaptivity

[1] Corresponding author: r.sevilla@swansea.ac.uk

1. Introduction

For the last two decades, the interest in high-order methods has grown considerably in many areas of science and engineering [1, 2, 3, 4]. High-order methods usually offer a substantial reduction in the number of degrees of freedom necessary to achieve a desired accuracy when compared to low-order methods [5, 6, 7, 8, 9, 10] and, in some occasions, also a reduction in the required computational time [11, 12].

In addition, high-order methods on unstructured meshes offer a better geometric representation of complex geometries [13, 14, 15] due to the possibility to employ curved elements. However, to exploit the benefits of high-order methods, the use of coarse meshes with large curved elements is mandatory and, very often, the accuracy of the resulting numerical methodology is compromised by the accuracy provided by the approximated boundary representation of curved elements [16, 17].

The so-called NURBS-enhanced finite element method (NEFEM) was introduced in [18] to remove the geometric uncertainty present in isoparametric elements and guarantee that the element size used in a finite element simulation is dictated by the requirements of the physics and not by the geometric complexity of a model. Its application to heat transfer, electromagnetic and fluid flow problems has been extensively studied in the last decade [18, 19], but its application to solid mechanics problems remains unexplored.

In this paper NEFEM is considered, for the first time, for the solution of solid mechanics problems. The two dimensional linear elastic case is considered and NEFEM is combined with a hybridisable discontinuous Galerkin (HDG) formulation [20, 21, 22, 23, 24, 25]. The proposed HDG-NEFEM

rationale presents three advantages compared to standard HDG methods. First, HDG-NEFEM is able to reproduce polynomial solutions of arbitrary order in domains with curved boundaries. Second, HDG-NEFEM enables to obtain a super-convergent approximation of the displacement field in domains with curved boundaries even for linear approximation, contrary to the standard HDG approach based on isoparametric elements. Third, HDG-NEFEM enables to devise degree adaptive procedures with no communication with a CAD system during the degree adaptive iterations, contrary to standard HDG methods with isoparametric elements. Two error indicators, based on the displacement and stress field respectively, are considered. The former has been explored for wave propagation and fluid flow problems whereas the latter has not been exploited in an HDG framework.

The rest of the paper is organised as follows. In Section 2 the elastic problem is introduced using the traditional Voigt notation. The HDG variational formulation is recalled in Section 3. The numerical solution strategy is discussed in detail in Section 4, with special emphasis in the differences between the traditional HDG method and the proposed HDG-NEFEM approach from a theoretical and a computational standpoint. The strategy to perform the degree adaptivity by using the super-convergent properties of the HDG formulation is recalled in Section 5, together with a novel alternative error indicator of the stress field by exploiting the mixed formulation employed in HDG. Four numerical examples are considered in Section 6 to illustrate the three main advantages of the proposed HDG-NEFEM approach and to illustrate its applicability in a setting involving a more complex geometry. Finally, Section 7 presents some concluding remarks.

2. Problem statement

The linear elastic behaviour a solid $\Omega \subset \mathbb{R}^2$, whose boundary $\partial\Omega$ has been split into the non-overlapping Dirichlet, Neumann and symmetry boundaries, Γ_D, Γ_N and Γ_S respectively, is governed by the boundary value problem

$$\begin{cases} -\boldsymbol{\nabla}\cdot\boldsymbol{\sigma} = \boldsymbol{f} & \text{in } \Omega, \\ \boldsymbol{u} = \boldsymbol{u}_D & \text{on } \Gamma_D, \\ \boldsymbol{n}\cdot\boldsymbol{\sigma} = \boldsymbol{g} & \text{on } \Gamma_N, \\ \mathbf{P}_n\boldsymbol{u} + \mathbf{P}_t\boldsymbol{n}\cdot\boldsymbol{\sigma} = \mathbf{0}, & \text{on } \Gamma_S, \end{cases} \tag{1}$$

where $\boldsymbol{\sigma}$ denotes the Cauchy stress tensor, $\boldsymbol{f}$ denotes an external force, $\boldsymbol{u}$ is the displacement field, $\boldsymbol{n}$ is the outward unit normal vector to $\partial\Omega$ and the normal and tangent projection matrices are defined over the symmetry boundary as $\mathbf{P}_n = \boldsymbol{n}\otimes\boldsymbol{n}$ and $\mathbf{P}_t = \mathbf{I}_2 - \boldsymbol{n}\otimes\boldsymbol{n}$ respectively. The boundary conditions are given by the imposed displacements on the Dirichlet boundary, $\boldsymbol{u}_D$, and the traction vector on the Neumann boundary, $\boldsymbol{g}$.

Assuming that the medium is linear elastic, the stress-strain relation given by the Hooke's law is used, namely $\boldsymbol{\sigma} = \mathbf{C}{:}\boldsymbol{\varepsilon}(\boldsymbol{u})$, where $\mathbf{C}$ is the fourth order elasticity tensor and the linearised strain tensor is $\boldsymbol{\varepsilon}(\boldsymbol{u}) := \left(\boldsymbol{\nabla}\boldsymbol{u} + \boldsymbol{\nabla}\boldsymbol{u}^T\right)/2$.

In this context, it is common to employ the so-called Voigt notation [26] to reduce the order of the stress and strain tensors by exploiting their symmetry. In two dimensions, the strain and stress vectors are defined as $\boldsymbol{\varepsilon}_{\mathtt{V}} := [\varepsilon_{11},\ \varepsilon_{22},\ \gamma_{12}]^T$ and $\boldsymbol{\sigma}_{\mathtt{V}} := [\sigma_{11},\ \sigma_{22},\ \tau_{12}]^T$ respectively. The strain vector is defined in terms of the displacement vector as $\boldsymbol{\varepsilon}_{\mathtt{V}} = \boldsymbol{\nabla}_{\mathtt{S}}\boldsymbol{u}$, where the

symmetric gradient matrix operator is given by

$$\boldsymbol{\nabla}_{\mathtt{S}} := \begin{bmatrix} \partial/\partial x_1 & 0 & \partial/\partial x_2 \\ 0 & \partial/\partial x_2 & \partial/\partial x_1 \end{bmatrix}^T . \tag{2}$$

Using the Voigt notation, the linear relation between strain and stress given by the Hooke's law is also simplified and it can be written as $\boldsymbol{\sigma}_{\mathtt{V}} = \mathbf{D}\boldsymbol{\varepsilon}_{\mathtt{V}}$, where $\mathbf{D}$ is a symmetric and positive definite matrix that is dependent on the hypothesis used to simplify the problem from three to two dimensions (i.e. plane strain or plane stress) and the material properties of the medium. This matrix is given by

$$\mathbf{D} := \frac{E}{(1+\nu)(1-\vartheta\nu)} \begin{bmatrix} 1+(1-\vartheta)\nu & \nu & 0 \\ \nu & 1+(1-\vartheta)\nu & 0 \\ 0 & 0 & (1-\vartheta\nu)/2 \end{bmatrix}, \tag{3}$$

where ϑ takes value 0 or 1 for a plane strain or plane stress model respectively, E is the Young modulus and ν is the Poisson ratio.

Finally, the linear elastic problem can be written in strong form with the Voigt notation as

$$\begin{cases} -\boldsymbol{\nabla}_{\mathtt{S}}^T \boldsymbol{\sigma}_{\mathtt{V}} = \boldsymbol{f} & \text{in } \Omega, \\ \boldsymbol{u} = \boldsymbol{u}_D & \text{on } \Gamma_D, \\ \mathbf{N}^T \boldsymbol{\sigma}_{\mathtt{V}} = \boldsymbol{g} & \text{on } \Gamma_N, \\ \mathbf{P}_n \boldsymbol{u} + \mathbf{P}_t \mathbf{N}^T \boldsymbol{\sigma}_{\mathtt{V}} = \mathbf{0} & \text{on } \Gamma_S, \end{cases} \tag{4}$$

where

$$\mathbf{N} := \begin{bmatrix} n_1 & 0 & n_2 \\ 0 & n_2 & n_1 \end{bmatrix}^T . \tag{5}$$

3. Hybridisable discontinuous Galerkin formulation

A regular partition of the domain Ω in triangular disjoint elements Ω_e with boundaries $\partial\Omega_e$ is considered and the set of interior edges Γ is defined as

$$\Gamma := \left[\bigcup_{e=1}^{\mathtt{n_{el}}} \partial\Omega_e\right] \setminus \partial\Omega. \tag{6}$$

It is assumed that the triangles have, at most, one edge on the boundary, which is assumed to be described by a collection of NURBS curves [27].

The following discrete element spaces are introduced

$$\mathcal{V}^h(\Omega) := \left\{v \in \mathcal{L}_2(\Omega) : v|_{\Omega_e} \in \mathcal{P}^{k_e}(\Omega_e) \forall \Omega_e\right\}, \tag{7a}$$

$$\hat{\mathcal{V}}^h(S) := \left\{\hat{v} \in \mathcal{L}_2(S) : \hat{v}|_{\Gamma_j} \in \mathcal{P}^{k_j}(\Gamma_j)\ \forall \Gamma_j \subset S \subseteq \Gamma \cup \Gamma_S\right\}, \tag{7b}$$

where $\mathcal{P}^{k_e}(\Omega_e)$ and $\mathcal{P}^{k_j}(\Gamma_j)$ denote the spaces of polynomials of degree at most k_e in Ω_e and k_j on Γ_j respectively. It is worth noting that, similar to other DG methods, the proposed approach easily allows to use different degree of approximation in different elements.

Finally, the standard internal products of vector functions in $\mathcal{L}_2(\Omega_e)$ and $\mathcal{L}_2(\Gamma_i)$ are also defined

$$(\boldsymbol{p}, \boldsymbol{q})_{\Omega_e} := \int_{\Omega_e} \boldsymbol{p} \cdot \boldsymbol{q}\ d\Omega, \qquad \langle \hat{\boldsymbol{p}}, \hat{\boldsymbol{q}} \rangle_{\partial\Omega_e} := \sum_{\Gamma_i \subset \partial\Omega_e} \int_{\Gamma_i} \hat{\boldsymbol{p}} \cdot \hat{\boldsymbol{q}}\ d\Gamma. \tag{8}$$

3.1. Local and global problems

Following the standard HDG rationale [20, 28, 23, 24, 29, 30, 31], a mixed formulation of the strong form of the elastic problem given by Equation (4)

is considered in each element, namely

$$\begin{cases} \boldsymbol{L} + \mathbf{D}^{1/2}\boldsymbol{\nabla}_{\mathtt{S}}\boldsymbol{u} = \mathbf{0} & \text{in } \Omega_e, \text{ and for } e = 1, \dots, \mathtt{n_{el}}, \\ \boldsymbol{\nabla}_{\mathtt{S}}^T\mathbf{D}^{1/2}\boldsymbol{L} = \boldsymbol{f} & \text{in } \Omega_e, \text{ and for } e = 1, \dots, \mathtt{n_{el}}, \\ \boldsymbol{u} = \boldsymbol{u}_D & \text{on } \Gamma_D, \\ \mathbf{N}^T\mathbf{D}^{1/2}\boldsymbol{L} = -\boldsymbol{g} & \text{on } \Gamma_N, \\ \mathbf{P}_n\boldsymbol{u} - \mathbf{P}_t\mathbf{N}^T\mathbf{D}^{1/2}\boldsymbol{L} = \mathbf{0} & \text{on } \Gamma_S, \\ [\![\boldsymbol{u} \otimes \boldsymbol{n}]\!] = \mathbf{0} & \text{on } \Gamma, \\ [\![\mathbf{N}^T\mathbf{D}^{1/2}\boldsymbol{L}]\!] = \mathbf{0} & \text{on } \Gamma, \end{cases} \tag{9}$$

where $[\![\odot]\!] = \odot_e + \odot_l$ denotes the jump over an interior edge shared by two elements and the last two equations in (9), usually referred to as *transmission conditions*, enforce the continuity of the solution and the normal stress across all the interior edges of the mesh.

Remark 1. *The matrix* $\mathbf{D}^{1/2}$ *has been introduced in Equation* (9) *to ensure that the resulting formulation leads to a symmetric system of equations after the spatial discretisation is introduced. This matrix is computed as* $\mathbf{D}^{1/2} = \mathbf{V}\boldsymbol{\Lambda}^{1/2}\mathbf{V}^T$*, where* $\mathbf{V}$ *and* $\boldsymbol{\Lambda}$ *are the matrices resulting from the eigen-decomposition of* $\mathbf{D}$ *.*

The HDG method splits Equation (9) into two problems. The so-called *local problem* is used to express the primal and dual variables in each element (i.e. $\boldsymbol{u}_e$ and $\boldsymbol{L}_e$) in terms of a hybrid variable defined over the interior edges

$\widehat{\boldsymbol{u}}$, namely

$$\begin{cases} \boldsymbol{L}_e + \mathbf{D}^{1/2}\boldsymbol{\nabla}_{\mathtt{S}}\boldsymbol{u}_e = \mathbf{0} & \text{in } \Omega_e, \text{ and for } e = 1, \ldots, \mathtt{n_{el}}, \\ \boldsymbol{\nabla}_{\mathtt{S}}^T\mathbf{D}^{1/2}\boldsymbol{L}_e = \boldsymbol{f} & \text{in } \Omega_e, \text{ and for } e = 1, \ldots, \mathtt{n_{el}}, \\ \boldsymbol{u}_e = \boldsymbol{u}_D & \text{on } \partial\Omega_e \cap \Gamma_D, \\ \mathbf{N}^T\mathbf{D}^{1/2}\boldsymbol{L}_e = -\boldsymbol{g} & \text{on } \partial\Omega_e \cap \Gamma_N, \\ \boldsymbol{u}_e = \widehat{\boldsymbol{u}} & \text{on } \partial\Omega_e \setminus (\Gamma_D \cup \Gamma_N). \end{cases} \tag{10}$$

Remark 2. *The local problem in Equation* (10) *incorporates the Neumann boundary conditions. This approach, proposed in [31], differs from the common practice in HDG methods [20, 28, 23, 24, 29, 30]. The main implication of this choice is that the hybrid variable* $\widehat{\boldsymbol{u}}$ *does not exist over the boundary of the computational domain. As this work is concerned with the approximation of solutions in domains with curved boundaries, the choice made implies that the hybrid variable is defined over straight internal edges only.*

Second, the so-called *global problem* is solved in order to obtain the approximation of the hybrid variable $\widehat{\boldsymbol{u}}$

$$\begin{cases} \mathbf{P}_n\boldsymbol{u}_e - \mathbf{P}_t\mathbf{N}^T\mathbf{D}^{1/2}\boldsymbol{L}_e = \mathbf{0} & \text{on } \Gamma_S, \\ [\![\mathbf{N}^T\mathbf{D}^{1/2}\boldsymbol{L}_e]\!] = \mathbf{0} & \text{on } \Gamma, \end{cases} \tag{11}$$

where the equation imposing the continuity of the displacement field in the interior edges is automatically satisfied due to the Dirichlet condition $\boldsymbol{u}_e = \widehat{\boldsymbol{u}}$ imposed in the local problems and the uniqueness of the hybrid variable in the interior edges.

3.2. Weak formulation

The discrete weak form of the local problem corresponding to Equation (10) is: given $\boldsymbol{f}$ in Ω, $\boldsymbol{u}_D$ on Γ_D, $\boldsymbol{g}$ on Γ_N and $\widehat{\boldsymbol{u}}$ on $\Gamma \cup \Gamma_S$, find

$(\boldsymbol{L}_e^h, \boldsymbol{u}_e^h) \in [\mathcal{V}^h(\Omega_e)]^3 \times [\mathcal{V}^h(\Omega_e)]^2$ such that

$$\begin{aligned} -(\boldsymbol{v}, \boldsymbol{L}_e^h)_{\Omega_e} + (\boldsymbol{\nabla}_{\mathtt{S}}^T \mathbf{D}^{1/2} \boldsymbol{v}, \boldsymbol{u}_e^h)_{\Omega_e} - \langle \mathbf{N}_e^T \mathbf{D}^{1/2} \boldsymbol{v}, \boldsymbol{u}_e^h \rangle_{\partial\Omega_e \cap \Gamma_N} \\ = \langle \mathbf{N}_e^T \mathbf{D}^{1/2} \boldsymbol{v}, \boldsymbol{u}_D \rangle_{\partial\Omega_e \cap \Gamma_D} + \langle \mathbf{N}_e^T \mathbf{D}^{1/2} \boldsymbol{v}, \widehat{\boldsymbol{u}}^h \rangle_{\partial\Omega_e \setminus (\Gamma_D \cup \Gamma_N)}, \end{aligned} \tag{12a}$$

$$-(\boldsymbol{\nabla}_{\mathtt{S}} \boldsymbol{w}, \mathbf{D}^{1/2} \boldsymbol{L}_e^h)_{\Omega_e} + \langle \boldsymbol{w}, \mathbf{N}_e^T \widehat{\mathbf{D}^{1/2} \boldsymbol{L}_e^h} \rangle_{\partial\Omega_e} = (\boldsymbol{w}, \boldsymbol{f})_{\Omega_e}, \tag{12b}$$

for all $(\boldsymbol{v}, \boldsymbol{w}) \in [\mathcal{V}^h(\Omega_e)]^3 \times [\mathcal{V}^h(\Omega_e)]^2$ and for each element $\Omega_e,\ e = 1, \ldots, \mathtt{n_{el}}$.

After performing a second integration by parts of the first term in Equation (12b) and introducing the numerical trace of the stress, defined by

$$\widehat{\mathbf{N}_e^T \mathbf{D}^{1/2} \boldsymbol{L}_e^h} := \begin{cases} \mathbf{N}_e^T \mathbf{D}^{1/2} \boldsymbol{L}_e^h + \boldsymbol{\tau}_e (\boldsymbol{u}_e^h - \boldsymbol{u}_D) & \text{on } \partial\Omega_e \cap \Gamma_D, \\ -\boldsymbol{g} & \text{on } \partial\Omega_e \cap \Gamma_N, \\ \mathbf{N}_e^T \mathbf{D}^{1/2} \boldsymbol{L}_e^h + \boldsymbol{\tau}_e (\boldsymbol{u}_e^h - \widehat{\boldsymbol{u}}^h) & \text{elsewhere,} \end{cases} \tag{13}$$

the discrete weak formulation of the local problem becomes: given $\boldsymbol{f}$ in Ω, $\boldsymbol{u}_D$ on Γ_D, $\boldsymbol{g}$ on Γ_N and $\widehat{\boldsymbol{u}}$ on $\Gamma \cup \Gamma_S$, find $(\boldsymbol{L}_e^h, \boldsymbol{u}_e^h) \in [\mathcal{V}^h(\Omega_e)]^3 \times [\mathcal{V}^h(\Omega_e)]^2$ such that

$$\begin{aligned} -(\boldsymbol{v}, \boldsymbol{L}_e^h)_{\Omega_e} + (\boldsymbol{\nabla}_{\mathtt{S}}^T \mathbf{D}^{1/2} \boldsymbol{v}, \boldsymbol{u}_e^h)_{\Omega_e} - \langle \mathbf{N}_e^T \mathbf{D}^{1/2} \boldsymbol{v}, \boldsymbol{u}_e^h \rangle_{\partial\Omega_e \cap \Gamma_N} \\ = \langle \mathbf{N}_e^T \mathbf{D}^{1/2} \boldsymbol{v}, \boldsymbol{u}_D \rangle_{\partial\Omega_e \cap \Gamma_D} + \langle \mathbf{N}_e^T \mathbf{D}^{1/2} \boldsymbol{v}, \widehat{\boldsymbol{u}}^h \rangle_{\partial\Omega_e \setminus (\Gamma_D \cup \Gamma_N)}, \end{aligned} \tag{14a}$$

$$\begin{aligned} (\boldsymbol{w}, \boldsymbol{\nabla}_{\mathtt{S}}^T \mathbf{D}^{1/2} \boldsymbol{L}_e^h)_{\Omega_e} - \langle \boldsymbol{w}, \mathbf{N}_e^T \mathbf{D}^{1/2} \boldsymbol{L}_e^h \rangle_{\partial\Omega_e \cap \Gamma_N} + \langle \boldsymbol{w}, \boldsymbol{\tau}_e \boldsymbol{u}_e^h \rangle_{\partial\Omega_e} = (\boldsymbol{w}, \boldsymbol{f})_{\Omega_e} \\ + \langle \boldsymbol{w}, \boldsymbol{\tau}_e \boldsymbol{u}_D \rangle_{\partial\Omega_e \cap \Gamma_D} + \langle \boldsymbol{w}, \boldsymbol{g} \rangle_{\partial\Omega_e \cap \Gamma_N} + \langle \boldsymbol{w}, \boldsymbol{\tau}_e \widehat{\boldsymbol{u}}^h \rangle_{\partial\Omega_e \setminus (\Gamma_D \cup \Gamma_N)}, \end{aligned} \tag{14b}$$

for all $(\boldsymbol{v}, \boldsymbol{w}) \in [\mathcal{V}^h(\Omega_e)]^3 \times [\mathcal{V}^h(\Omega_e)]^2$ and for each element $\Omega_e,\ e = 1, \ldots, \mathtt{n_{el}}$.

The stabilisation tensor in Equation (13), $\boldsymbol{\tau}_e$, is introduced to ensure the stability and convergence of the resulting numerical scheme [20, 32]. The influence of this parameter in the accuracy of the method has been extensively

studied in [25, 33, 34]. Following [35], the stabilisation tensor is selected as $\boldsymbol{\tau}_e = (E/\ell)\mathbf{I}_2$, where ℓ is a characteristic length and $\mathbf{I}_2$ is the identity matrix of dimension two.

Analogously, the discrete weak form of the global problem corresponding to Equation (11) is: find $\widehat{\boldsymbol{u}}^h \in [\hat{\mathcal{V}}^h(\Gamma \cup \Gamma_S)]^2$ such that

$$\sum_{e=1}^{\mathtt{n_{el}}} \Big\{ \langle \widehat{\boldsymbol{w}}, \mathbf{N}_e^T \mathbf{D}^{1/2} \boldsymbol{L}_e^h \rangle_{\partial\Omega_e \setminus \partial\Omega} - \langle \widehat{\boldsymbol{w}}, \mathbf{P}_t \mathbf{N}_e^T \mathbf{D}^{1/2} \boldsymbol{L}_e^h \rangle_{\partial\Omega_e \cap \Gamma_S} + \langle \widehat{\boldsymbol{w}}, \boldsymbol{\tau}_e \boldsymbol{u}_e^h \rangle_{\partial\Omega_e \setminus \partial\Omega}$$
$$- \langle \widehat{\boldsymbol{w}}, \mathbf{P}_t \boldsymbol{\tau}_e \boldsymbol{u}_e^h \rangle_{\partial\Omega_e \cap \Gamma_S} - \langle \widehat{\boldsymbol{w}}, \boldsymbol{\tau}_e \widehat{\boldsymbol{u}}^h \rangle_{\partial\Omega_e \setminus \partial\Omega} + \langle \widehat{\boldsymbol{w}}, (\mathbf{P}_n + \mathbf{P}_t \boldsymbol{\tau}_e)\, \widehat{\boldsymbol{u}}^h \rangle_{\partial\Omega_e \cap \Gamma_S} \Big\} = 0, \tag{15}$$

for all $\widehat{\boldsymbol{w}} \in [\hat{\mathcal{V}}^h(\Gamma \cup \Gamma_N)]^{\mathtt{n_{sd}}}$.

4. Numerical solution

4.1. Spatial discretisation

The traditional isoparametric formulation defines the approximation of the primal and mixed variables, $\boldsymbol{u}_e^h$ and $\boldsymbol{L}_e^h$, in a reference element, with coordinates $\boldsymbol{\xi} = (\xi_1, \xi_2)$ as

$$\boldsymbol{u}^h(\boldsymbol{\xi}) = \sum_{j=1}^{\mathtt{n_{en}}} \mathbf{u}_j^{\mathrm{Iso}} N_j^{\mathrm{Iso}}(\boldsymbol{\xi}), \qquad \boldsymbol{L}^h(\boldsymbol{\xi}) = \sum_{j=1}^{\mathtt{n_{en}}} \mathbf{L}_j^{\mathrm{Iso}} N_j^{\mathrm{Iso}}(\boldsymbol{\xi}), \tag{16}$$

where $\mathbf{u}_j^{\mathrm{Iso}}$ and $\mathbf{L}_j^{\mathrm{Iso}}$ denote the nodal values of the primal and mixed variables, $\mathtt{n_{en}} = (k+1)(k+2)/2$ is the number of element nodes and N_j^{Iso} are the Lagrangian polynomials of order k defined in the reference triangle [17].

The proposed HDG-NEFEM approach differs from the classical isoparametric approach in the treatment of the elements in contact with curved boundaries [18, 36]. In those elements, the approximation of the primal and

mixed variables is defined directly in the physical space, with coordinates $\boldsymbol{x} = (x_1, x_2)$ as

$$\boldsymbol{u}^h(\boldsymbol{x}) = \sum_{j=1}^{\mathtt{n_{en}}} \mathbf{u}_j^{\mathrm{Phy}} N_j^{\mathrm{Phy}}(\boldsymbol{x}), \qquad \boldsymbol{L}^h(\boldsymbol{x}) = \sum_{j=1}^{\mathtt{n_{en}}} \mathbf{L}_j^{\mathrm{Phy}} N_j^{\mathrm{Phy}}(\boldsymbol{x}), \tag{17}$$

where $\mathbf{u}_j^{\mathrm{Phy}}$ and $\mathbf{L}_j^{\mathrm{Phy}}$ denote the nodal values of the primal and mixed variables and N_j^{Phy} are the Lagrangian polynomials of order k defined in the physical element. For the elements with at most one node on the curved boundary, the HDG-NEFEM approach considers the same approximation as for an isoparametric element.

It is worth noting that, due to the HDG formulation considered here, with the Neumann boundary conditions introduced in the local problem of Equation (10) as detailed in Remark 2, the hybrid variable is not defined on curved boundaries. Therefore, for both the isoparametric HDG and the proposed HDG-NEFEM, the approximation of the hybrid variable, $\widehat{\boldsymbol{u}}^h$, is defined in a reference interval, with coordinates ξ as

$$\widehat{\boldsymbol{u}}^h(\xi) = \sum_{j=1}^{\mathtt{n_{fn}}} \hat{\mathbf{u}}_j N_j^{\mathrm{1D}}(\xi), \tag{18}$$

where $\hat{\mathbf{u}}_j$ denotes the nodal values of the hybrid variable, $\mathtt{n_{fn}} = (k+1)$ is the number of edge nodes and N_j^{1D} are the one-dimensional Lagrangian polynomials of order k defined in the reference face.

By introducing the approximations given by Equations (16) and (18) or Equations (17) and (18), for isoparametric or NEFEM respectively, in the discrete weak formulation of Equation (14), the following system of equations is obtained

$$\begin{bmatrix} \mathbf{A}_{LL} & \mathbf{A}_{Lu} \\ \mathbf{A}_{Lu}^T & \mathbf{A}_{uu} \end{bmatrix}_e \begin{Bmatrix} \mathbf{L}_e \\ \mathbf{u}_e \end{Bmatrix} = \begin{Bmatrix} \mathbf{f}_L \\ \mathbf{f}_u \end{Bmatrix}_e + \begin{bmatrix} \mathbf{A}_{L\hat{u}} \\ \mathbf{A}_{u\hat{u}} \end{bmatrix}_e \hat{\mathbf{u}}_e, \tag{19}$$

for each element $\Omega_e,\ e = 1, \ldots, \mathtt{n_{el}}$.

Analogously, introducing the approximations given by Equations (16) and (18) or Equations (17) and (18), for isoparametric or NEFEM respectively, in the discrete weak formulation of Equation (15), leads to the following system of equations

$$\sum_{e=1}^{\mathtt{n_{el}}} \left\{ \begin{bmatrix} \mathbf{A}_{L\hat{u}}^T & \mathbf{A}_{u\hat{u}}^T \end{bmatrix}_e \begin{Bmatrix} \mathbf{L}_e \\ \mathbf{u}_e \end{Bmatrix} + [\mathbf{A}_{\hat{u}\hat{u}}]_e \, \hat{\mathbf{u}}_e \right\} = \sum_{i=e}^{\mathtt{n_{el}}} [\mathbf{f}_{\hat{u}}]_e. \tag{20}$$

Finally, by using Equation (19) to express the nodal values of the primal and mixed variables in terms of the nodal values of the hybrid variable and introducing these expressions in the discrete form of the global problem, the following system of linear equations is obtained

$$\widehat{\mathbf{K}}\hat{\mathbf{u}} = \hat{\mathbf{f}}, \tag{21}$$

where

$$\widehat{\mathbf{K}} = \mathbf{A}_{e=1}^{\mathtt{n_{el}}} \begin{bmatrix} \mathbf{A}_{L\hat{u}}^T & \mathbf{A}_{u\hat{u}}^T \end{bmatrix}_e \begin{bmatrix} \mathbf{A}_{LL} & \mathbf{A}_{Lu} \\ \mathbf{A}_{Lu}^T & \mathbf{A}_{uu} \end{bmatrix}_e^{-1} \begin{bmatrix} \mathbf{A}_{L\hat{u}} \\ \mathbf{A}_{u\hat{u}} \end{bmatrix}_e + [\mathbf{A}_{\hat{u}\hat{u}}]_e \tag{22a}$$

and

$$\hat{\mathbf{f}} = \mathbf{A}_{e=1}^{\mathtt{n_{el}}} [\mathbf{f}_{\hat{u}}]_e - \begin{bmatrix} \mathbf{A}_{L\hat{u}}^T & \mathbf{A}_{u\hat{u}}^T \end{bmatrix}_e \begin{bmatrix} \mathbf{A}_{LL} & \mathbf{A}_{Lu} \\ \mathbf{A}_{Lu}^T & \mathbf{A}_{uu} \end{bmatrix}_e^{-1} \begin{Bmatrix} \mathbf{f}_L \\ \mathbf{f}_u \end{Bmatrix}_e . \tag{22b}$$

Remark 3. *The symmetry of the local and global systems is guaranteed due to the use of the eigendecomposition of the matrix* $\mathbf{D}$ *introduced in Equation* (9).

4.2. Computational aspects

To illustrate the differences between the standard isoparametric and the proposed NEFEM approaches, the computation of two terms of the weak

formulation involving an integral in a curved element and an integral in a curved edge are considered.

The term $\mathbf{A}_{LL}$, involving the integral $(\boldsymbol{v}, \boldsymbol{L}^h)_{\Omega_e}$, is considered first. For a curved isoparametric element, the integral is computed as

$$\begin{aligned}\left(\boldsymbol{v}, \boldsymbol{L}^h\right)_{\Omega_e} = \left(\boldsymbol{v}, \boldsymbol{L}^h|\mathbf{J}_{\boldsymbol{\varphi}}|\right)_{\Omega_{\text{Ref}}} &= \sum_{j=1}^{\mathtt{n}_{\mathtt{en}}} \left(\mathbf{M}(\boldsymbol{\xi}), \mathbf{M}(\boldsymbol{\xi})|\mathbf{J}_{\boldsymbol{\varphi}}|\right)_{\Omega_{\text{Ref}}} \mathbf{L}_j^{\text{Iso}} \\ &\approx \sum_{j=1}^{\mathtt{n}_{\mathtt{en}}} \left[\sum_{\mathtt{g}=1}^{\mathtt{n}_{\mathtt{eip}}^{\text{Ref}}} \mathbf{M}(\boldsymbol{\xi}_{\mathtt{g}}^{\text{Ref}}) \mathbf{M}^T(\boldsymbol{\xi}_{\mathtt{g}}^{\text{Ref}}) |\mathbf{J}_{\boldsymbol{\varphi}}(\boldsymbol{\xi}_{\mathtt{g}}^{\text{Ref}})| w_{\mathtt{g}}^{\text{Ref}} \right] \mathbf{L}_j^{\text{Iso}},\end{aligned} \tag{23}$$

where $\mathbf{M}(\boldsymbol{\xi}) = [N_1^{\text{Iso}}(\boldsymbol{\xi})\mathbf{I}_3, N_2^{\text{Iso}}(\boldsymbol{\xi})\mathbf{I}_3, \ldots, N_{\mathtt{n}_{\mathtt{en}}}^{\text{Iso}}(\boldsymbol{\xi})\mathbf{I}_3]^T$, $\mathbf{J}_{\boldsymbol{\varphi}}$ denotes the Jacobian of the isoparametric mapping, used to transform the integral to the reference triangle Ω_{Ref}, and $\{(\boldsymbol{\xi}_{\mathtt{g}}^{\text{Ref}}, w_{\mathtt{g}}^{\text{Ref}})\}$ is the set of $\mathtt{n}_{\mathtt{eip}}^{\text{Ref}}$ integration points and weights in Ω_{Ref}.

For the proposed HDG-NEFEM, the term $\mathbf{A}_{LL}$, is computed as

$$\begin{aligned}(\boldsymbol{v}, \boldsymbol{L}^h)_{\Omega_e} &= \sum_{j=1}^{\mathtt{n}_{\mathtt{en}}} (\mathbf{M}(\boldsymbol{x}), \mathbf{M}(\boldsymbol{x})_j(\boldsymbol{x}))_{\Omega_e} \mathbf{L}_j^{\text{Phys}} \\ &\approx \sum_{j=1}^{\mathtt{n}_{\mathtt{en}}} \left[\sum_{\mathtt{g}=1}^{\mathtt{n}_{\mathtt{eip}}^{\text{Phys}}} \mathbf{M}(\boldsymbol{x}_{\mathtt{g}}^{\text{Phys}}) \mathbf{M}^T(\boldsymbol{x}_{\mathtt{g}}^{\text{Phys}}) w_{\mathtt{g}}^{\text{Phys}} \right] \mathbf{L}_j^{\text{Phys}},\end{aligned} \tag{24}$$

where $\mathbf{M}(\boldsymbol{x}) = [N_1^{\text{Phys}}(\boldsymbol{x})\mathbf{I}_3, N_2^{\text{Phys}}(\boldsymbol{x})\mathbf{I}_3, \ldots, N_{\mathtt{n}_{\mathtt{en}}}^{\text{Phys}}(\boldsymbol{x})\mathbf{I}_3]^T$ and $\{(\boldsymbol{x}^{\text{Phys}}, w_{\mathtt{g}}^{\text{Phys}})\}$ is the set of $\mathtt{n}_{\mathtt{eip}}^{\text{Phys}}$ integration points and weights in Ω_e, constructed using the strategy proposed in [37].

The term $\mathbf{A}_{uu}$, involving the integral $\langle \boldsymbol{w}, \boldsymbol{\tau}_e \boldsymbol{u}_e^h \rangle_{\Gamma_e}$ is considered next. For

a curved isoparametric edge, the integral is computed as

$$\begin{aligned}\langle \boldsymbol{w}, \boldsymbol{\tau}_e \boldsymbol{u}_e^h \rangle_{\Gamma_e} &= \langle \boldsymbol{w}, \boldsymbol{\tau}_e \boldsymbol{u}_e^h \|\Psi'\| \rangle_{\Gamma_{\text{Ref}}} = \sum_{j=1}^{\mathtt{n_{fn}}} \langle \mathbf{m}(\xi, \mathbf{I}_2), \mathbf{m}(\xi, \boldsymbol{\tau}_e) \|\Psi'\| \rangle_{\Gamma_{\text{Ref}}} \mathbf{u}_j^{\text{Iso}} \\ &\approx \sum_{j=1}^{\mathtt{n_{fn}}} \left[\sum_{\mathtt{g}=1}^{\mathtt{n}_{\mathtt{fip}}^{\text{Ref}}} \mathbf{m}(\xi_g^{\text{Ref}}, \mathbf{I}_2) \mathbf{m}^T(\xi_g^{\text{Ref}}, \boldsymbol{\tau}_e) \|\Psi'(\xi_g^{\text{Ref}})\| \omega_g^{\text{Ref}} \right] \mathbf{u}_j^{\text{Iso}},\end{aligned} \tag{25}$$

where $\mathbf{m}(\xi, \mathbf{A}) = [N_1^{1\text{D}}(\boldsymbol{\xi})\mathbf{A}, N_2^{1\text{D}}(\boldsymbol{\xi})\mathbf{A}, \ldots, N_{\mathtt{n_{fn}}}^{1\text{D}}(\boldsymbol{\xi})\mathbf{A}]^T$, Ψ denotes the isoparametric mapping used to transform the integral to the reference edge Γ_{Ref}, and $\{(\xi_g^{\text{Ref}}, \omega_g^{\text{Ref}})\}$ is the set of $\mathtt{n}_{\mathtt{fip}}^{\text{Ref}}$ integration points and weights in Γ_{Ref}.

For the proposed HDG-NEFEM, the term $\mathbf{A}_{uu}$, is computed as

$$\begin{aligned}\langle \boldsymbol{w}, \boldsymbol{\tau}_e \boldsymbol{u}_e^h \rangle_{\Gamma_e} &= \sum_{j=1}^{\mathtt{n_{en}}} \langle \mathbf{m}(\boldsymbol{x}, \mathbf{I}_2), \mathbf{m}(\boldsymbol{x}, \boldsymbol{\tau}_e) \rangle_{\Gamma_e} \mathbf{u}_j^{\text{Phys}} \\ &\approx \sum_{j=1}^{\mathtt{n_{en}}} \left[\sum_{\mathtt{g}=1}^{\mathtt{n}_{\mathtt{fip}}^{\text{Phys}}} \mathbf{m}(\xi_g^{\text{Phys}}, \mathbf{I}_2) \mathbf{m}^T(\xi_g^{\text{Phys}}, \boldsymbol{\tau}_e) \omega_g^{\text{Phys}} \right] \mathbf{u}_j^{\text{Phys}},\end{aligned} \tag{26}$$

where $\mathbf{m}(\boldsymbol{x}, \mathbf{A}) = [N_1^{\text{Phys}}(\boldsymbol{x})\mathbf{A}, N_2^{\text{Phys}}(\boldsymbol{x})\mathbf{A}, \ldots, N_{\mathtt{n_{en}}}^{\text{Phys}}(\boldsymbol{x})\mathbf{A}]^T$ and $\{(\boldsymbol{x}_g^{\text{Phys}}, \omega_g^{\text{Phys}})\}$ is the set of $\mathtt{n}_{\mathtt{fip}}^{\text{Phys}}$ integration points and weights in Γ_e, constructed using the strategy proposed in [37].

Remark 4. *There are two important differences between the classical isoparametric approach and the proposed NEFEM rationale. First, in NEFEM, the shape functions in NEFEM are constructed directly in the physical space, rather than in a reference element. This means that the quality of the approximation is less sensitive to element distortion because the Jacobian of the isoparametric mapping does not feature in the integrals. There is also more flexibility when placing the nodes in a NEFEM elements [36], but to*

ensure a fair comparison the nodes for both isoparametric and NEFEM elements are always placed in the same position. In addition, this implies that the summation in the edge integrals include all element nodes and not just the edge nodes as it is common in the isoparametric formulation. Second, the quadratures in NEFEM are tailored to the element by accounting for the NURBS boundary description of the computational domain.

5. Degree adaptivity

Two strategies for driving the degree adaptive process are described here. The first one is based on the super-convergent properties of the HDG method and has recently being exploited in order to devise cheap and reliable error indicators for fluid and wave problems [38, 39, 40]. The second option proposed in this paper relies on the mixed formulation employed by HDG methods and is more attractive when the quantity of interest is the stress field rather than the displacement field.

5.1. Degree adaptivity driven by the displacement field

An attractive feature of the HDG method is the possibility to perform an element-by-element postprocess of the solution to obtain a better approximation of the displacement field [20, 28, 29, 30, 41]. The postprocess considered here solves the following problem in each element

$$\begin{cases} \boldsymbol{\nabla}_{\mathtt{S}}^T \mathbf{D}^{1/2} \boldsymbol{\nabla}_{\mathtt{S}} \boldsymbol{u}_e^\star = -\boldsymbol{\nabla}_{\mathtt{S}}^T \boldsymbol{L}_e & \text{in } \Omega_e,\ e = 1, \dots, \mathtt{n_{el}}, \\ \mathbf{N}^T \mathbf{D}^{1/2} \boldsymbol{\nabla}_{\mathtt{S}} \boldsymbol{u}_e^\star = -\mathbf{N}^T \boldsymbol{L}_e & \text{on } \partial\Omega_e. \end{cases} \tag{27}$$

where $\boldsymbol{u}_e^\star$ is the postprocessed solution. To ensure the uniqueness of the solution, the two conditions

$$\int_{\Omega_e} \boldsymbol{u}_e^\star \, d\Omega = \int_{\Omega_e} \boldsymbol{u}_e^h \, d\Omega. \tag{28}$$

$$\int_{\Omega_e} \boldsymbol{\nabla} \times \boldsymbol{u}_e^\star \, d\Omega = \int_{\partial\Omega_e} \widehat{\boldsymbol{u}}^h \cdot \boldsymbol{t}_e \, d\Gamma, \tag{29}$$

are enforced to remove the translation and rotational modes respectively, where $\boldsymbol{t}_e$ denotes the tangent vector to the boundary of the element. The second condition, introduced for the first time in [35], guarantees the superconvergence of the solution for any order of approximation $k \geq 1$.

The ability to produce a better approximation of the primal variable has recently being exploited in order to devise cheap and reliable error indicators for fluid and wave problems [38, 39, 40]. The main idea consists of building an error indicator in each element as

$$E_e^u = \left[\frac{1}{|\Omega_e|} \int_{\Omega_e} (\boldsymbol{u}^\star - \boldsymbol{u}) \cdot (\boldsymbol{u}^\star - \boldsymbol{u}) \, d\Omega \right]^{1/2}, \tag{30}$$

and utilise the local *a priori* error estimate, valid for elliptic problems, described in [42], namely

$$\varepsilon_e^u = \|\boldsymbol{u} - \boldsymbol{u}_h\|_{\Omega_e} \leq C h_e^{k_e+2}, \tag{31}$$

in two dimensions, where C is a constant, h_e is the characteristic size of the element Ω_e and k_e is the polynomial degree of approximation employed in Ω_e.

A simple Richardson extrapolation can then be applied to estimate the change in the degree of approximation required in each element to guarantee that the estimated error is below a desired error ε^u, namely

$$\Delta k_e^u = \left\lceil \frac{\log(\varepsilon^u / E_e^u)}{\log(h_e)} \right\rceil, \tag{32}$$

where $\lceil \cdot \rceil$ is the ceiling function.

5.2. Degree adaptivity driven by the stress field

The second exploits the fact that the primal and mixed variables, $\boldsymbol{u}$ and $\boldsymbol{L}$ respectively, are treated as independent variables but they are related by the first Equation in (9) due to the mixed formulation employed in HDG.

The main idea is to exploit the better approximation properties of $\boldsymbol{L}$, approximated with polynomials of degree k, when compared to $-\mathbf{D}^{1/2}\boldsymbol{\nabla}_{\mathtt{S}}\boldsymbol{u}$, which is approximated with polynomials of degree $k-1$. Therefore, an error indicator for the stress in each element is given by

$$E_e^{\sigma} = \left[\frac{1}{|\Omega_e|} \int_{\Omega_e} \left(\mathbf{D}\boldsymbol{\nabla}_{\mathtt{S}}\boldsymbol{u} + \mathbf{D}^{1/2}\boldsymbol{L} \right) \cdot \left(\mathbf{D}\boldsymbol{\nabla}_{\mathtt{S}}\boldsymbol{u} + \mathbf{D}^{1/2}\boldsymbol{L} \right) d\Omega \right]^{1/2}, \tag{33}$$

By utilising the local *a priori* error estimate in [42] and Richardson extrapolation, the following expression for the change in the degree of approximation required in each element to guarantee that the estimated error is below a desired error ε^{σ}, namely

$$\Delta k_e^{\sigma} = \left\lceil \frac{\log(\varepsilon^{\sigma}/E_e^{\sigma})}{\log(h_e)} \right\rceil. \tag{34}$$

The main advantage of the indicator based on stress is that the element by element postprocess of the displacement described in Equation (27) is avoided. In addition, it is worth noting that a third error indicator could be devised by combining both the indicators presented in this Section.

6. Numerical examples

6.1. Patch tests

The first example is used to demonstrate the ability of the proposed HDG-NEFEM method to pass the low and higher order patch tests (i.e. to exactly

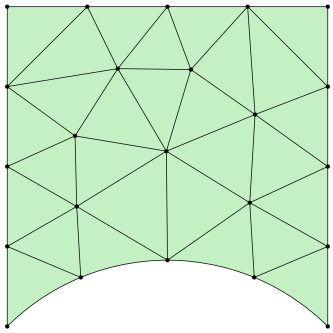

Figure 1: Coarse mesh used in the patch tests.

reproduce polynomials) in domains with curved boundaries.

A coarse mesh with 28 triangular elements is considered to discretise the domain Ω, as shown in Figure 1. The model problem of Equation (4) is solved imposing Neumann boundary conditions on the bottom part of the boundary, which corresponds to a circle with centre $[0.5, -0.5]$ and radius $\sqrt{2}/2$, and Dirichlet boundary conditions in the rest of the boundary.

Two cases are considered with linear and quadratic analytical solution, namely $\boldsymbol{u}(\boldsymbol{x}) = (x_1 + 2x_2, \quad x_2 - x_1)$ and $\boldsymbol{u}(\boldsymbol{x}) = (x_1^2 + x_2^2, \quad x_2^2 - 2x_1 + 4)$, respectively.

Figure 2 shows the evolution of the error of the displacement and the stress fields as a function of the degree of the functional approximation for both isoparametric HDG and HDG-NEFEM. The results clearly demonstrate that with an approximation of degree k, HDG-NEFEM is able to approximate polynomial solution of degree k with machine accuracy, whereas the isoparametric HDG approach is not able to reproduce polynomial solutions in domains with curved boundaries. This is due to the inability of isoparametric elements to describe the circular boundary exactly and, for quadratic

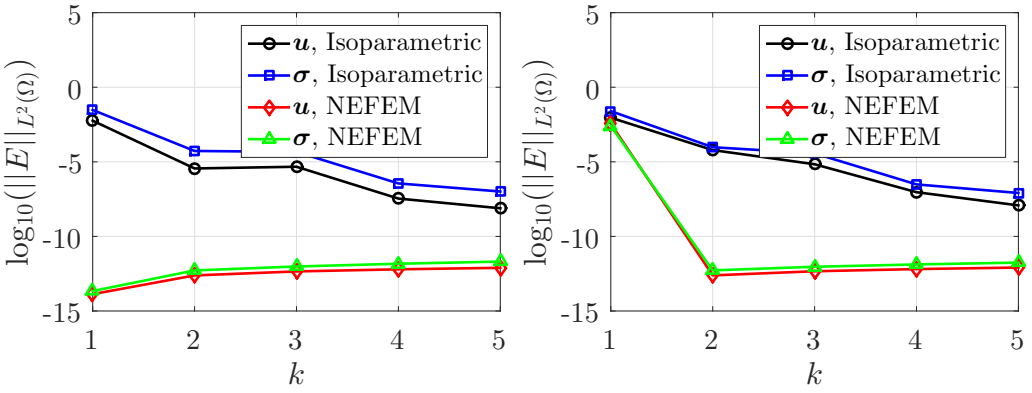

(a) Linear (b) Quadratic

Figure 2: Patch tests: Convergence of the error of the displacement and stress in the $\mathcal{L}_2(\Omega)$ norm as a function of the degree of approximation for isoparametric HDG and HDG-NEFEM for a problem with analytical solution being a linear and quadratic function.

or high-order elements, due to the definition of the polynomial approximation in the reference element rather than in the physical space. The non-linear character of the isoparametric mapping leads to an approximation in the physical space that avoids to exactly reproduce polynomials.

6.2. Lamé problem

The next example, usually referred to as the Lamé problem [43, 44, 45], considers a thick-walled infinite cylinder under uniform pressure. Using the symmetry of the problem, only a quarter of the two dimensional section is considered, as depicted in Figure 3. Neumann boundary conditions, corresponding to a uniform pressure p_i and p_o, are applied on the inner ($r = r_i$) and outer ($r = r_o$) part of the boundary respectively. Symmetry boundary conditions are considered on the boundaries aligned with the axis. A material with Young modulus $E = 1$ and Poisson ratio $\nu = 0.3$ is considered and

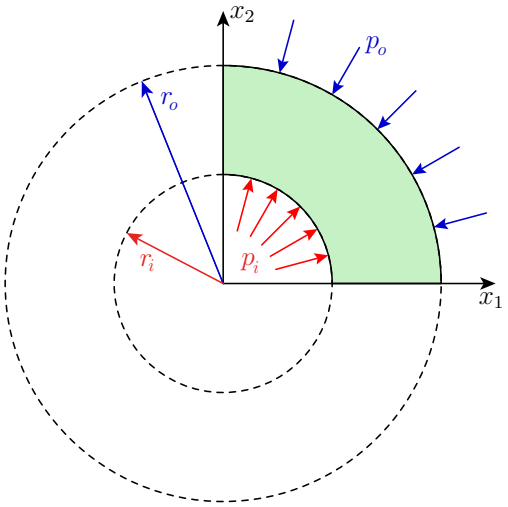

Figure 3: Lamé problem.

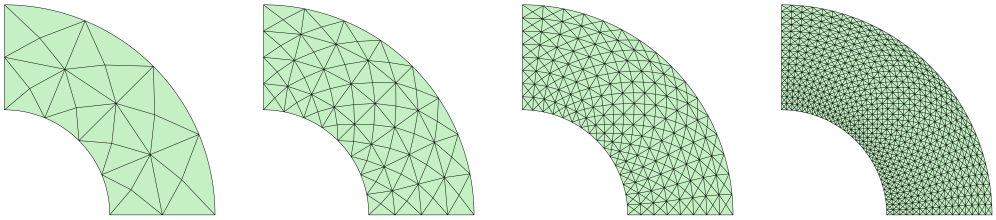

(a) Mesh 1 (b) Mesh 2 (c) Mesh 3 (d) Mesh 4

Figure 4: Lamé problem: Four triangular successively refined meshes.

the plane strain hypothesis is assumed. The dimensions of the domain are given by $r_i = 1$ and $r_o = 2$ and the imposed pressure is $p_i = 1$ and $p_o = 0.5$.

This classical test case is used to check the optimal approximation properties of the proposed HDG-NEFEM methodology and to compare the accuracy against the classical HDG with isoparametric elements. To this end, a series of successively refined triangular meshes are considered. The first four meshes are represented in Figure 4. The high-order curved isoparametric

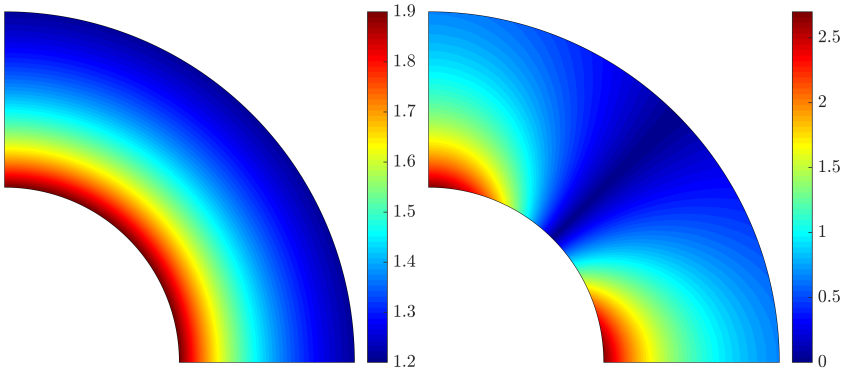

(a) Radial displacement (b) Von Mises stress

Figure 5: Lamé problem: HDG-NEFEM solution on the triangular mesh of Figure 4(d) with $k = 1$.

meshes are generated using the strategy described in [46, 47] with an extra constraint to ensure that the internal triangular edges are not deformed. The NEFEM meshes are generated using the technique proposed in [48].

The radial displacement and Von Mises stress, computed using the proposed HDG-NEFEM approach on the fourth mesh with a linear approximation ($k = 1$) of the solution, are represented in Figure 5. The computed solution is in excellent agreement with the analytical solution, with the relative error of the displacement field and the stress field in the $\mathcal{L}_2(\Omega)$ being 1.1×10^{-4} and 1.4×10^{-3} respectively.

Figure 6 shows the $\mathcal{L}_2(\Omega)$ norm of the error of the displacement field as a function of the characteristic element size h for both isoparametric and NEFEM elements and for a degree of approximation $k = 1, 2, 3$. The expected optimal rate of convergence (i.e, k+1) is observed in all cases. It is worth noting the extra accuracy provided by the NEFEM rationale when a linear approximation of the solution is considered. This difference is attributed to

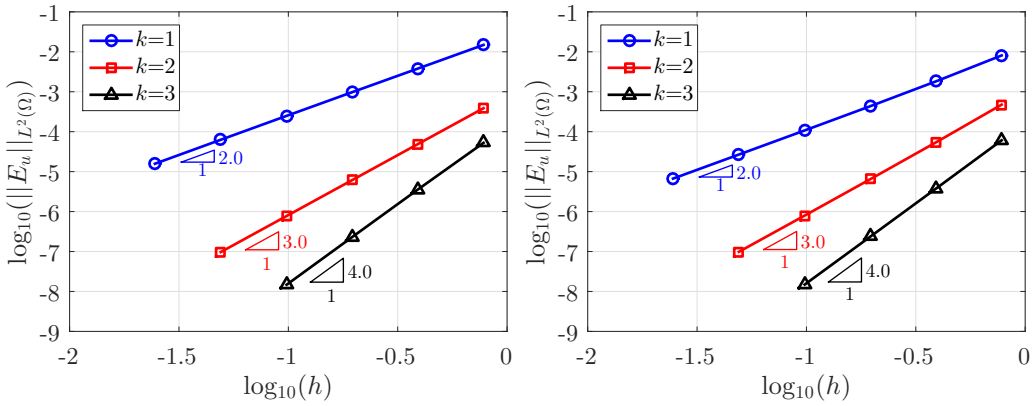

(a) HDG isoparametric

(b) HDG-NEFEM

Figure 6: Lamé problem: h-convergence of the $\mathcal{L}_2(\Omega)$ norm of the error of the displacement field as a function of the characteristic element size h for different values of the approximation degree k.

the polygonal description of the curved boundaries employed in the isoparametric formulation. For higher order approximations, the geometric error is lower than the interpolation error and the accuracy of both isoparametric and NEFEM elements is almost identical.

Figure 7 shows the $\mathcal{L}_2(\Omega)$ norm of the error of the stress field as a function of the characteristic element size h for both isoparametric and NEFEM elements and for a degree of approximation $k = 1, 2, 3$. For linear elements, the isoparametric formulation leads to a suboptimal rate of convergence whereas the incorporation of the exact geometry with NEFEM allows to recover the optimal rate of convergence of the error on the stress field. In this example, for the finest mesh with $k = 1$, NEFEM provides one order of magnitude more accurate results than the standard linear elements. This sizeable difference is attributed to the geometric error and to the non-physical singularity

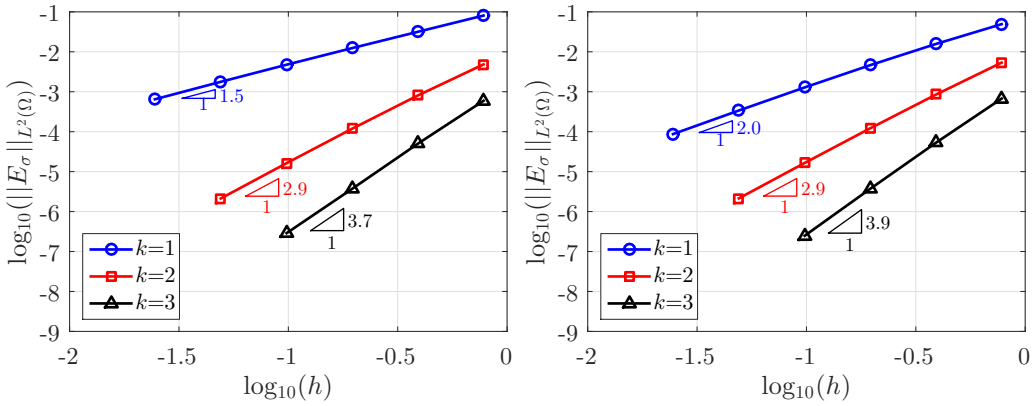

(a) HDG isoparametric

(b) HDG-NEFEM

Figure 7: Lamé problem: h-convergence of the $\mathcal{L}_2(\Omega)$ norm of the error of the stress field as a function of the characteristic element size h for different values of the approximation degree k.

that a polygonal approximation of the boundary induces on the stress field. It is worth noting that the extra loss of accuracy on the stress field is partially attributed to the non-physical singularities introduced by a polygonal representation of the boundary because this is effect is only observed on the stress field and not on the displacement field, which converges optimally. For quadratic elements both the isoparametric and the NEFEM formulations provide similar accuracy and almost the optimal rate of convergence $k+1$. Finally, for cubic elements almost the same accuracy is provided by isoparametric and NEFEM elements, despite a marginal loss on the convergence rate is observed for the isoparametric approach.

Finally, Figure 8 shows the $\mathcal{L}_2(\Omega)$ norm of the error of the post-processed displacement field as a function of the characteristic element size h for both isoparametric and NEFEM elements and for a degree of approximation $k =$

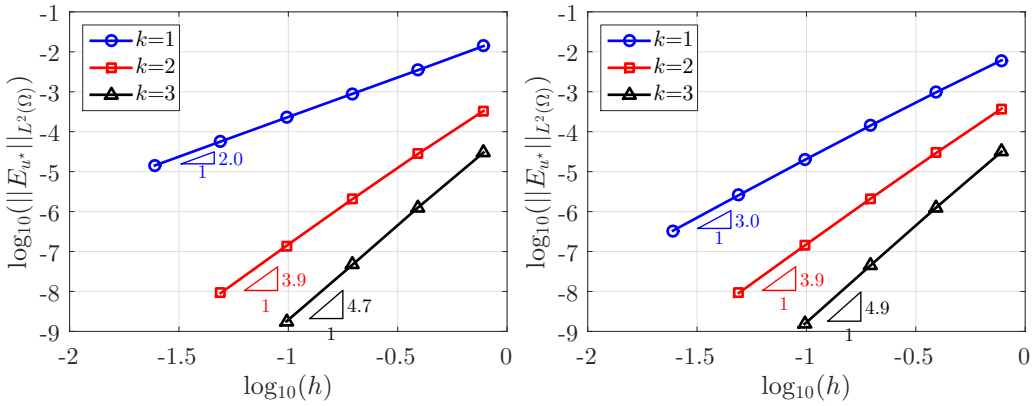

(a) HDG isoparametric

(b) HDG-NEFEM

Figure 8: Lamé problem: h-convergence of the $\mathcal{L}_2(\Omega)$ norm of the error of the post-processed displacement field as a function of the characteristic element size h for different values of the approximation degree k.

$1, 2, 3$. The results show that with linear isoparametric elements it is not possible to recover the optimal rate of convergence $k+2$, whereas the NEFEM approach provides the optimal convergence. The sub-optimal rate of convergence of the isoparametric approach is due to the polygonal approximation of the boundary. In this case, the geometric error converges with order 2, preventing the error of the numerical solution to converge faster. For higher orders of approximation almost identical accuracy and nearly the optimal rate of convergence is observed for both isoparametric and NEFEM elements. In this case the geometric error introduced in the isoparametric approach converges with order $2k$ which, for $k \geq 2$ is greater than or equal to $k+2$.

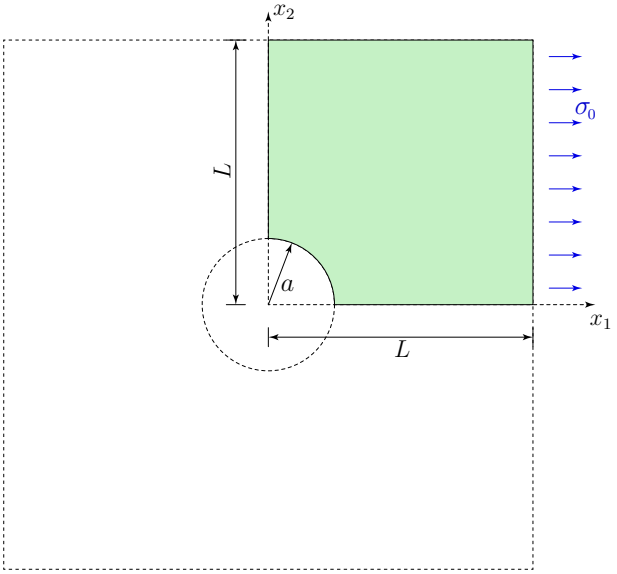

Figure 9: Kirsch problem.

6.3. Kirsch problem

The next example considers another classical test case for linear elastic solvers, the so-called Kirsch's problem [43, 44, 45]. This example involves the computation of the displacement and stress fields in an infinite plate with a circular hole loaded under a uniform tension σ_0 in the horizontal direction. Using the symmetry of the problem, only a quarter of the plate is considered, as depicted in Figure 9. Homogeneous Neumann boundary conditions are imposed on the circular part of the boundary and Neumann boundary conditions, corresponding to the analytical tension, are imposed on the right and top part of the plate to avoid any effect from the truncation of the infinite plate. Symmetry boundary conditions are considered on the boundaries aligned with the axis. A material with Young modulus $E = 1$ and Poisson ratio $\nu = 0.3$ is considered and the plane stress hypothesis is

assumed. The dimensions of the domain are given by $L = 4$, $a = 1$ and the imposed traction is $\sigma_0 = 10$.

This test case is used to show the advantages of the proposed HDG-NEFEM formulation within a degree adaptive process driven by the displacement based error indicator in Section 5.1. A coarse mesh is fixed and the degree of approximation in each element is automatically changed to guarantee that the error of the computed displacement field is below a pre-defined tolerance.

Figure 10 shows the evolution of the estimated and exact error as a function of the number of iterations of the degree adaptive process for both standard HDG and HDG-NEFEM. For the standard HDG approach three different cases are analysed corresponding to a linear ($q = 1$), quadratic($q = 2$) and cubic ($q = 3$) description of the curved boundary respectively. As described in [40], this initial choice of the boundary representation of the curved boundary is required to avoid communication with the CAD and mesh generation systems in each iteration of the degree adaptive process.

The results clearly demonstrate that with the standard HDG method, there is a significant discrepancy between the estimated and the exact error. In this case, the exact error stagnates after one or two iterations of the adaptive process whereas the estimated error converges to the desired value, leading to a final solution where the indicator does not reflect the true error of the computation. To better illustrate the discrepancy between the estimated and exact errors, Figure 11 shows the final degree of approximation as dictated by the adaptive process and the exact and the estimated errors for an HDG computation with a cubic representation of the curved boundary

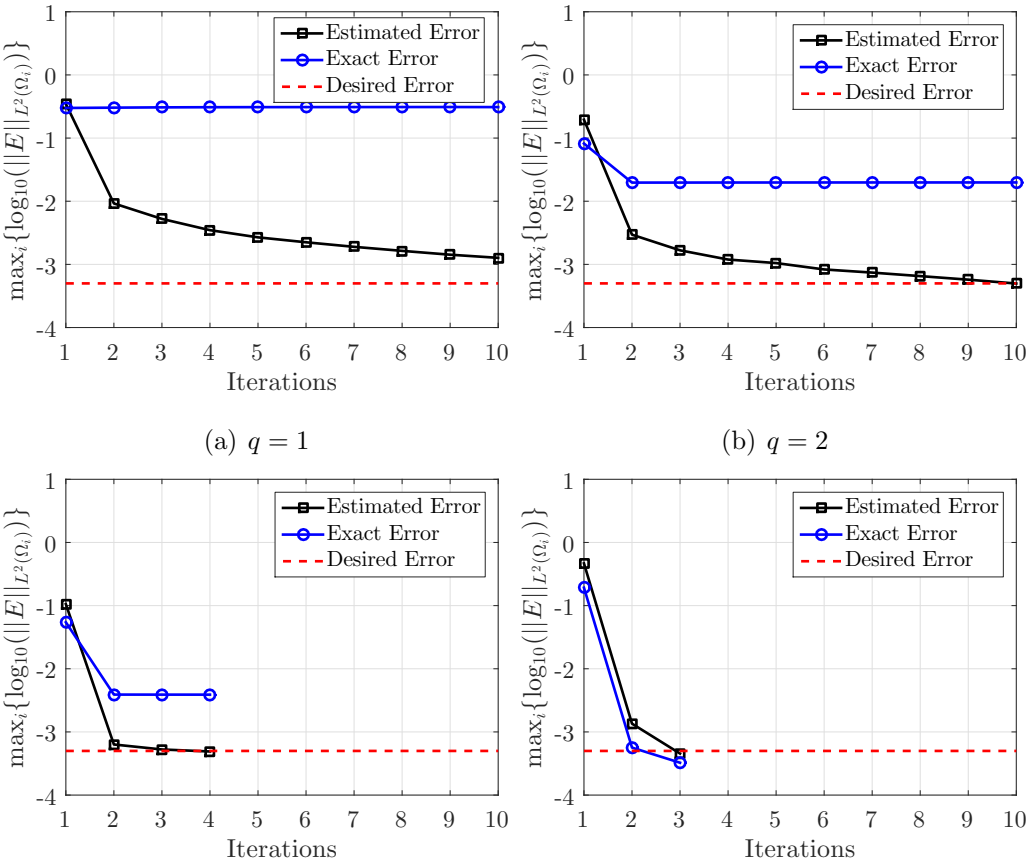

(a) $q = 1$ (b) $q = 2$

(c) $q = 3$ (d) NEFEM

Figure 10: Kirsch problem: evolution of the estimated and exact errors as a function of the number of iterations of the degree adaptive process for standard HDG and HDG-NEFEM. The desired error is $\varepsilon_e^u = 0.5 \times 10^{-3}$.

($q = 3$). It is worth noting that the discrepancy between exact and estimated errors is not restricted to the elements in contact with the curved boundary.

In contrast, with HDG-NEFEM, the estimated and exact error are extremely close in each iteration of the adaptive process and, with only three iterations, the computed solution provides the desired accuracy. Figure 12

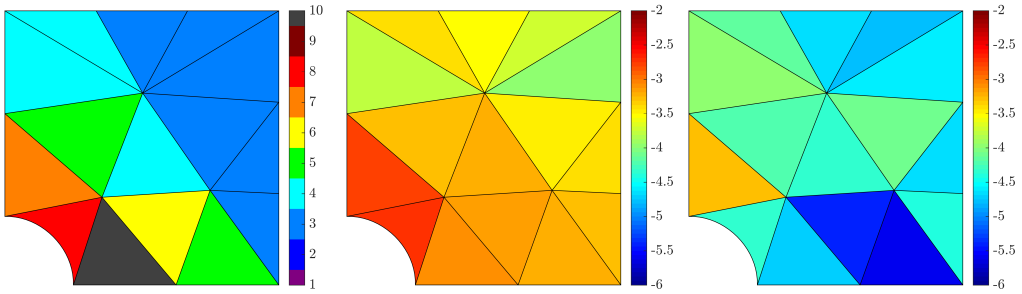

(a) Degree distribution (b) Exact error (c) Estimated error

Figure 11: Kirsch problem: HDG adaptive computation with a cubic representation of the curved boundary for a desired error of $\varepsilon_e^u = 0.5 \times 10^{-3}$.

shows the final degree of approximation as dictated by the adaptive process and the exact and the estimated errors for the HDG-NEFEM computation. The good correspondence between the estimated and exact error can be clearly observed. The final computation of the degree adaptive process

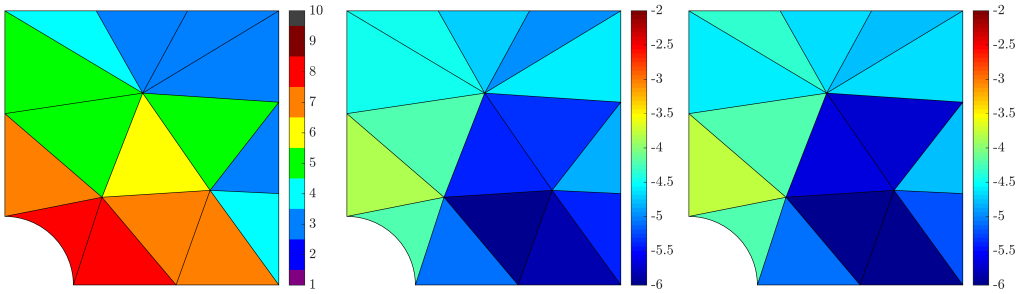

(a) Degree distribution (b) Exact error (c) Estimated error

Figure 12: Kirsch problem: HDG-NEFEM adaptive computation for a desired error of $\varepsilon_e^u = 0.5 \times 10^{-3}$.

with HDG-NEFEM exhibits a maximum elemental error of the displacement field is 0.33×10^{-3}, below the specified tolerance of $\varepsilon_e^u = 0.5 \times 10^{-3}$.

The stress field computed with HDG-NEFEM and the degree of approx-

imation distribution shown in Figure 12 (a) is depicted in Figure 13. It is

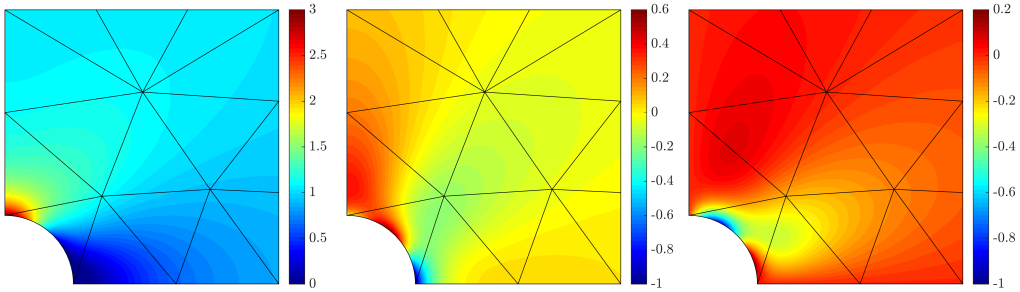

(a) σ_{11} (b) σ_{22} (c) σ_{12}

Figure 13: Kirsch problem: computed stress field with the HDG-NEFEM approach and the degree of approximation distribution shown in Figure 12 (a).

worth noting the ability of the proposed HDG-NEFEM approach to capture the variation of the stress field near the curved boundary, with only curved element.

Finally, to better illustrate the benefit of the proposed HDG-NEFEM, Figure 14 shows the evolution of the maximum stress σ_{11} as a function of the number of iterations of the degree adaptive process for the standard HDG with linear ($q = 1$), quadratic($q = 2$) and cubic ($q = 3$) description of the curved boundary and for the proposed HDG-NEFEM. The results show that an excellent agreement with the exact value if achieved with HDG-NEFEM whereas the maximum stress is overestimated with a polynomial representation of the boundary. The overestimated value obtained with the standard HDG approach is caused by the lack of $\mathcal{C}^1$ continuity of the boundary representation. At the mesh vertices situated on the curved boundary, the polynomial representation (for any degree q) is continuous but the derivative is discontinuous, creating a corner that induces a singularity in the stress field.

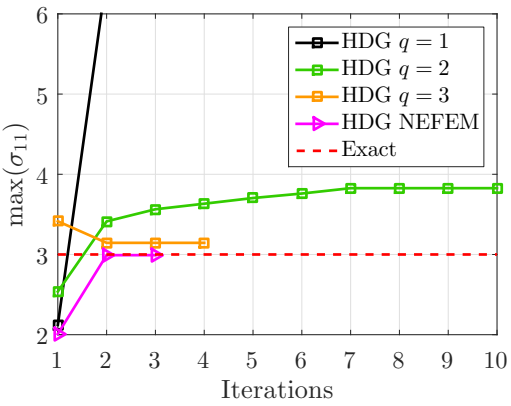

Figure 14: Evolution of the maximum stress σ_{11} as a function of the iterations of the degree adaptive process for the standard HDG approach with a linear, quadratic and cubic representation of the curved boundary and for HDG-NEFEM.

The NURBS boundary representation incorporated in the HDG-NEFEM approach ensures a smooth boundary representation and leads to a high fidelity stress field computation. It is worth recalling that the problem solved here considers only a quarter of the plate, as shown in Figure 9. Therefore if the normal to the curved boundary at points $(a, 0)$ and $(0, a)$ is not parallel to the x and y axis respectively, as it happens in the isoparametric HDG, the problem simulated in the domain using a symmetry boundary condition represents a problem with a non-smooth boundary representation with singularities. This also explains why in the adaptive process with isoparametric elements there is one element with only one node on the boundary with an extremely high degree of approximation, $k = 10$.

6.4. Flying wheel

The last example considers a more complicated geometry corresponding to a flying wheel, as depicted in Figure 15. The wheel is subject to an imposed

traction of magnitude 10^4 Pa on the outer boundary and it is fixed on the largest inner circle, whereas free traction is considered on the remaining part of the boundary. The material properties, corresponding to aluminium, are $E = 70$ GPa and $\nu = 0.33$.

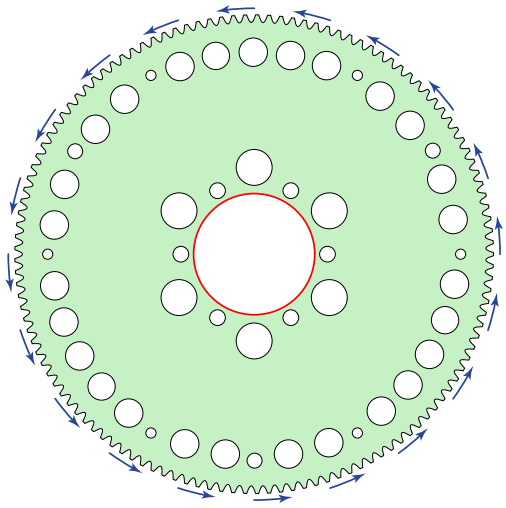

Figure 15: Flying wheel.

This test case is used to demonstrate the potential of the proposed HDG-NEFEM formulation within a degree adaptive process driven by the stress based error indicator in Section 5.2. The mesh shown in Figure 16 (a), with 16,651 triangular elements, is considered. The process starts with a uniform linear approximation of the solution and the desired error is $\varepsilon_e^\sigma = 0.5 \times 10^{-3}$. After five iterations the degree of approximation required in each element to guarantee that the error is below ε_e^σ is represented in Figure 16 (b). The solution computed on this mesh requires the solution of a global system of 52,168 equations and the computed components of the stress field are shown in Figure 17.

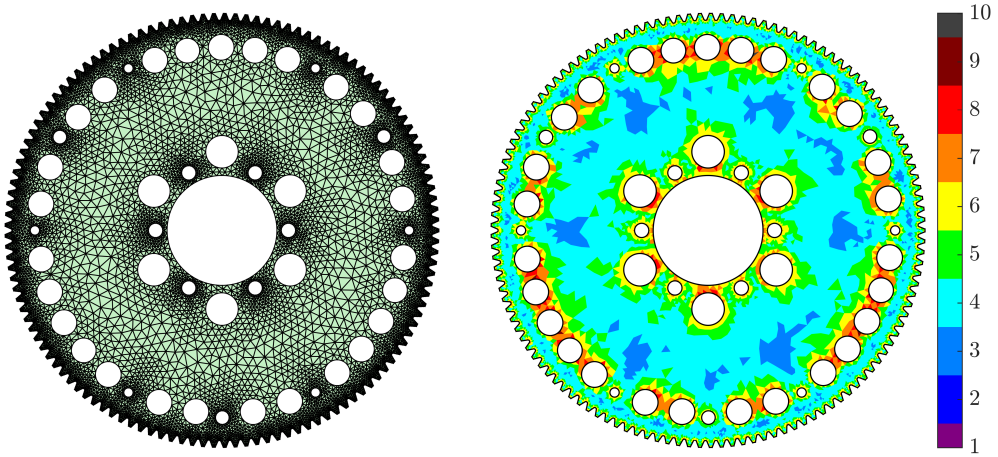

Figure 16: Flying wheel: degree distribution for an HDG-NEFEM adaptive computation with $\varepsilon_e^\sigma = 0.5 \times 10^{-3}$.

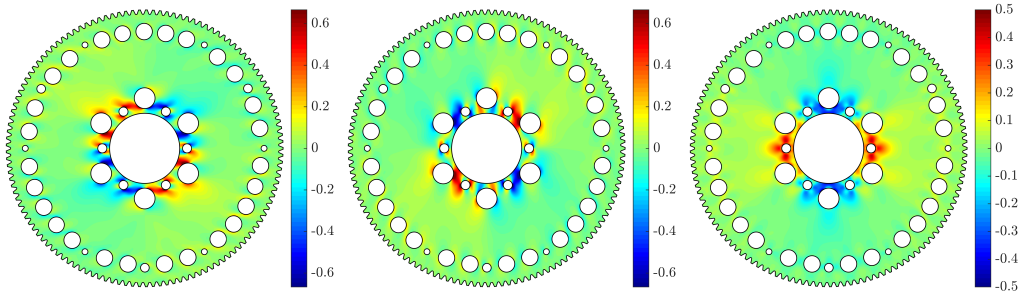

(a) σ_{11} (b) σ_{22} (c) σ_{12}

Figure 17: Flying wheel: computed stress field with the HDG-NEFEM approach and the degree of approximation distribution shown in Figure 16.

The maximum computed values of the stress components σ_{11}, σ_{22} and σ_{12} are 1.1816×10^4 Pa, 1.2312×10^4 Pa and 0.6323×10^4 Pa respectively. As no analytical solution is available, a reference solution is computed on a very fine mesh, with 113,539 triangular elements and with a uniform degree of approximation $k = 6$. The simulation required the solution of a global system

of 347,190 equations and the maximum computed values of the stress components σ_{11}, σ_{22} and σ_{12} are 1.1820×10^4 Pa, 1.2311×10^4 Pa, and 0.6323×10^4 Pa respectively. This example demonstrates the ability of the proposed degree adaptivity process driven by the stress field to provide highly accurate results by combining the exact boundary representation of NEFEM.

7. Concluding remarks

A combined HDG-NEFEM methodology for the solution of two dimensional linear elastic problems has been presented. The proposed methodology considers the application of the NEFEM rationale to solid mechanics problems for the first time. The combined HDG-NEFEM approach enables to reproduce polynomial solutions of any degree and to obtain a super-convergent solution when a linear approximation of the solution is considered. In contrast, the isoparametric HDG is not able to reproduce polynomial solutions in domains with curved boundaries and it shows a sub-optimal convergence of the post-processed variable due to the dominance of the geometric error.

The application of the proposed HDG-NEFEM methodology in a degree adaptive process is also presented. The exact boundary representation considered with a NEFEM rationale provides reliable error indicators for domains with curved boundaries and, contrary to standard isoparametric HDG elements, enables the computation of the solution with the required accuracy without communicating with a CAD system. Numerical examples are used to demonstrate the advantages of the proposed HDG-NEFEM approach combined with an error indicator for the displacement field and a new strategy to estimate the error on the stress field.

The extension to three dimensional problems does not introduce a conceptual difficulty but extra attention must be paid to the NEFEM mesh generation [48]. Finally, the extension to non-linear problems only needs a standard linearisation but it requires a careful selection of the stability parameter of the HDG formulation [49].

Acknowledgements

This work is partially supported by the European Union's Horizon 2020 research and innovation programme under the Marie Skłodowska–Curie actions (Grant number: 675919).

References

[1] K. Christodoulou, O. Laghrouche, M. Mohamed, J. Trevelyan, High-order finite elements for the solution of Helmholtz problems, Computers & Structures 191 (2017) 129–139.

[2] R. Sevilla, A. J. Gil, M. Weberstadt, A high-order stabilised ALE finite element formulation for the Euler equations on deformable domains, Computers & Structures 181 (2017) 89–102.

[3] D. Xu, Y. Yang, H. Zheng, A. Wu, A high order local approximation free from linear dependency with quadrilateral mesh as mathematical cover and applications to linear elastic fractures, Computers & Structures 178 (2017) 1–16.

[4] E. Brodal, J. S. Hesthaven, F. Melandsø, Numerical modeling of double-layered piezoelectric transducer systems using a high-order discontinuous Galerkin method, Computers & Structures 86 (2008) 1747–1756.

[5] B. Szabó, I. Babuška, Finite Element Analysis, John Wiley & Sons, New York, 1991.

[6] R. Kirby, S. J. Sherwin, B. Cockburn, To CG or to HDG: A comparative study, Journal of Scientific Computing 51 (2011) 183–212.

[7] A. Huerta, A. Angeloski, X. Roca, J. Peraire, Efficiency of high-order elements for continuous and discontinuous Galerkin methods, International Journal for Numerical Methods in Engineering 96 (2013) 529–560.

[8] G. Giorgiani, D. Modesto, S. Fernández-Méndez, A. Huerta, High-order continuous and discontinuous galerkin methods for wave problems, International Journal for numerical methods in Fluids 73 (2013) 883–903.

[9] S. Yakovlev, D. Moxey, R. M. Kirby, S. J. Sherwin, To CG or to HDG: a comparative study in 3d, Journal of Scientific Computing 67 (2016) 192–220.

[10] H. Bériot, A. Prinn, G. Gabard, Efficient implementation of high-order finite elements for Helmholtz problems, International Journal for Numerical Methods in Engineering 106 (2016) 213–240.

[11] R. Sevilla, O. Hassan, K. Morgan, An analysis of the performance of a high-order stabilised finite element method for simulating compressible flows, Computer Methods in Applied Mechanics and Engineering 253 (2013) 15–27.

[12] R. Sevilla, O. Hassan, K. Morgan, The use of hybrid meshes to improve the efficiency of a discontinuous Galerkin method for the solution of Maxwell's equations, Computers & Structures 137 (2014) 2–13.

[13] S. Dey, M. S. Shephard, J. E. Flaherty, Geometry representation issues associated with p-version finite element computations, Computer Methods in Applied Mechanics and Engineering 150 (1997) 39–55.

[14] F. Bassi, S. Rebay, High-order accurate discontinuous finite element solution of the 2D Euler equations, Journal of Computational Physics 138 (1997) 251–285.

[15] L. Krivodonova, M. Berger, High-order accurate implementation of solid wall boundary conditions in curved geometries, Journal of computational physics 211 (2006) 492–512.

[16] D. Xue, L. Demkowicz, et al., Control of geometry induced error in hp finite element (FE) simulations. I. Evaluation of FE error for curvilinear geometries, International Journal of Numerical Analysis and Modeling 2 (2005) 283–300.

[17] R. Sevilla, S. Fernández−Méndez, A. Huerta, Comparison of high-order curved finite elements, International Journal for Numerical Methods in Engineering 87 (2011) 719–734.

[18] R. Sevilla, S. Fernández−Méndez, A. Huerta, NURBS–enhanced finite element method (NEFEM), International Journal for Numerical Methods in Engineering 76 (2008) 56–83.

[19] R. Sevilla, S. Fernández-Méndez, A. Huerta, NURBS-enhanced finite element method (NEFEM) for Euler equations, International Journal for Numerical Methods in Fluids 57 (2008) 1051–1069.

[20] B. Cockburn, J. Gopalakrishnan, R. Lazarov, Unified hybridization of discontinuous Galerkin, mixed, and continuous Galerkin methods for second order elliptic problems, SIAM Journal on Numerical Analysis 47 (2009) 1319–1365.

[21] B. Cockburn, B. Dong, J. Guzmán, M. Restelli, R. Sacco, A hybridizable discontinuous Galerkin method for steady-state convection-diffusion-reaction problems, SIAM Journal on Scientific Computing 31 (2009) 3827–3846.

[22] B. Cockburn, J. Gopalakrishnan, The derivation of hybridizable discontinuous galerkin methods for stokes flow, SIAM Journal on Numerical Analysis 47 (2009) 1092–1125.

[23] N. C. Nguyen, J. Peraire, B. Cockburn, An implicit high-order hybridizable discontinuous Galerkin method for linear convection-diffusion equations, Journal of Computational Physics 228 (2009) 3232–3254.

[24] N. C. Nguyen, J. Peraire, B. Cockburn, An implicit high-order hybridizable discontinuous Galerkin method for nonlinear convection-diffusion equations, Journal of Computational Physics 228 (2009) 8841–8855.

[25] B. Cockburn, K. Shi, Superconvergent HDG methods for linear elasticity with weakly symmetric stresses, IMA Journal of Numerical Analysis 33 (2012) 747–770.

[26] J. Fish, T. Belytschko, A First Course in Finite Elements, John Wiley & Sons, 2007.

[27] L. Piegl, W. Tiller, The NURBS book, Springer Science & Business Media, 2012.

[28] B. Cockburn, B. Dong, J. Guzmán, A superconvergent LDG-hybridizable Galerkin method for second-order elliptic problems, Mathematics of Computation 77 (2008) 1887–1916.

[29] N. Nguyen, J. Peraire, B. Cockburn, A hybridizable discontinuous Galerkin method for Stokes flow, Computer Methods in Applied Mechanics and Engineering 199 (2010) 582–597.

[30] N. C. Nguyen, J. Peraire, B. Cockburn, An implicit high-order hybridizable discontinuous Galerkin method for the incompressible Navier-Stokes equations, Journal of Computational Physics 230 (2011) 1147–1170.

[31] R. Sevilla, A. Huerta, Tutorial on Hybridizable Discontinuous Galerkin (HDG) for second-order elliptic problems, in: J. Schröder, P. Wriggers (Eds.), Advanced Finite Element Technologies, volume 566 of *CISM International Centre for Mechanical Sciences*, Springer International Publishing, 2016, pp. 105–129.

[32] B. Cockburn, J. Guzmán, H. Wang, Superconvergent discontinuous Galerkin methods for second-order elliptic problems, Mathematics of Computation 78 (2009) 1–24.

[33] R. Sevilla, M. Giacomini, A. Huerta, A face-centred finite volume method for second-order elliptic problems, International Journal for Numerical Methods in Engineering 115 (2018) 986–1014.

[34] W. Qiu, J. Shen, K. Shi, An HDG method for linear elasticity with strong symmetric stresses, Mathematics of Computation 87 (2018) 69–93.

[35] R. Sevilla, M. Giacomini, A. Karkoulias, A. Huerta, A superconvergent hybridisable discontinuous galerkin method for linear elasticity, International Journal for Numerical Methods in Engineering 116 (2018) 91–116.

[36] R. Sevilla, S. Fernández−Méndez, A. Huerta, NURBS–Enhanced Finite Element Method (NEFEM): a seamless bridge between CAD and FEM, Archives of Computational Methods in Engineering 18 (2011) 441–484.

[37] R. Sevilla, S. Fernández-Méndez, Numerical integration over 2D NURBS shaped domains with applications to NURBS-enhanced FEM, Finite Elements in Analysis and Design 47 (2011) 1209–1220.

[38] G. Giorgiani, S. Fernández-Méndez, A. Huerta, Hybridizable discontinuous Galerkin p-adaptivity for wave propagation problems, International Journal for Numerical Methods in Fluids 72 (2013) 1244–1262.

[39] G. Giorgiani, S. Fernández-Méndez, A. Huerta, Hybridizable discontinuous Galerkin with degree adaptivity for the incompressible Navier-Stokes equations, Computers & Fluids 98 (2014) 196–208.

[40] R. Sevilla, A. Huerta, HDG-NEFEM with degree adaptivity for Stokes flows, Journal of Scientific Computing 77 (2018) 1953–1980.

[41] B. Cockburn, W. Qiu, K. Shi, Conditions for superconvergence of HDG methods for second-order elliptic problems, Mathematics of Computation 81 (2012) 1327–1353.

[42] P. Díez, A. Huerta, A unified approach to remeshing strategies for finite element h-adaptivity, Computer Methods in Applied Mechanics and Engineering 176 (1999) 215–229.

[43] S. P. Timoshenko, J. N. Goodier, Theory of elasticity, volume 3, McGraw-Hill, New York London, 1970.

[44] M. H. Sadd, Elasticity: theory, applications, and numerics, Academic Press, 2009.

[45] A. S. Saada, Elasticity: theory and applications, volume 16, Elsevier, 2013.

[46] Z. Q. Xie, R. Sevilla, O. Hassan, K. Morgan, The generation of arbitrary order curved meshes for 3D finite element analysis, Computational Mechanics 51 (2013) 361–374.

[47] R. Poya, R. Sevilla, A. J. Gil, A unified approach for a posteriori high-order curved mesh generation using solid mechanics, Computational Mechanics 58 (2016) 457–490.

[48] R. Sevilla, L. Rees, O. Hassan, The generation of triangular meshes for NURBS-enhanced FEM, International Journal for Numerical Methods in Engineering 108 (2016) 941–968.

[49] B. Cockburn, J. Shen, An algorithm for stabilizing hybridizable discontinuous Galerkin method for nonlinear elasticity, Results in Applied Mathematics (2019) 100001.